Available online at www.sciencedirect.com
SCIENCE DIRECT®
Optics Communications 246 (2005) 471–493
OPTICS COMMUNICATIONS
www.elsevier.com/locate/optcom

Global view of nonlinear dynamics in coupled-cavity lasers – a bifurcation study

Sebastian Wieczorek *, Weng W. Chow

Semiconductor Material and Device Sciences, Sandia National Laboratories, P.O. Box 5800, MS 0601, Albuquerque, NM 87185-0601, USA

Received 3 August 2004; received in revised form 29 October 2004; accepted 2 November 2004

Abstract

This paper investigates nonlinear behavior of coupled lasers. Composite-cavity-mode approach and a class-B description of the active medium are used to describe nonlinearities associated with population dynamics and optical coupling. The multimode equations are studied using bifurcation analysis to identify regions of stable locking, periodic oscillations, and complicated dynamics in the parameter space of coupling-mirror transmission T and normalized cavity-length mismatch dL/λ. We further investigate the evolution of the key bifurcations with the linewidth enhancement factor α. In particular, our analysis reveals the formation of a gap in the lockband that is gradually occupied by instabilities. We also investigate effects of the cavity-length on chaotic dynamics.

PACS: 42.55Px; 42.60Da; 42.65Sf; 05.45+b
Keywords: Coupled lasers; Composite-cavity mode theory; Multimode lasers; Semiconductor lasers; Bifurcations

1. Introduction

Coupled-laser systems have been a subject of intensive studies for four decades [1–3]. The primary interest was to investigate phase locking [4–8] for applications such as high-power light emission and frequency stabilization. Also, coupled-cavity (C^3) semiconductor lasers were proposed as candidates for high-speed applications [9]. More recently, coupled lasers were recognized for interesting nonlinear dynamics and chaos [10–13] which are the focus of present investigations. The majority of coupled-laser problems involve semiconductor lasers [14–24]. These widely used lasers are particularly sensitive to external perturbations due to a population-induced refractive-index

* Corresponding author. Tel.: +1 505 284 3388; fax: +1 505 844 3211.
E-mail address: smwiecz@sandia.gov (S. Wieczorek).

0030-4018/$ - see front matter © 2004 Elsevier B.V. All rights reserved.
doi:10.1016/j.optcom.2004.11.007

effect that couples the amplitude and the phase variations of the lasing field. As a result, coupled semiconductor lasers show rich displays of nonlinear dynamics that are not fully understood. While problems such as high-power light emission [25,26] and fast self pulsation [27,28] are still of interest, new applications appeared which require, instead of avoid erratic laser operation. Chaotic laser dynamics are used for secure communication [29] and for generating wave patterns in chaotic radars [30]. Moreover, coupled-laser effects lead to problems of cross-talk between electro-optic elements integrated onto a chip. Hence, development in the field of micro-optical circuits also requires fundamental and detailed understanding of dynamical complexities in coupled laser systems.

Studies of coupled lasers vary with respect to models, analytical, and numerical techniques [3,6,18,31–36]. On the one hand, multimode coupled lasers are described with partial differential equations [35,36], which is rigorous but does not allow bifurcation analysis nor the covering of large regions of parameter space. Simpler models assume a spatio-temporal electric field that can be factorized into space-dependent and time-dependent parts [37]. This reduces the wave equation to a set of ordinary differential equations for the modal amplitudes, and Helmholtz equation for the cavity modes. In coupled-laser problems, there are two approaches to modal expansion. In an individual-cavity theory [11–13,23], the coupling between resonators is neglected in the calculation of the cavity eigenmodes and each laser is described by the modes of the individual cavity. The electric field equation for each laser consists of the free-running laser part plus phenomenologically added fields (in the form of driving forces) from neighboring lasers. When lasers are coupled at a distance, an appropriate time delay is introduced in the coupling fields [16,19]. Such an approach has been widely applied to study synchronization under weak coupling conditions [16,38,39]. In an alternate approach, called the composite-cavity theory, coupling between the resonators is included in the passive modes, which are eigenmodes for the entire coupled-laser structure [6,31,32]. Resulting equations describe the evolution of electric fields associated with composite-cavity modes rather than with individual lasers. In terms of electric field treatment for coupled-laser problems, composite-cavity mode approach fills the gap between rigorous but computationally demanding models based on partial differential equations and phenomenological models derived from individual-cavity theory.

During the past years, considerable research has been devoted to coupled lasers with instantaneous [23,24,40,41] and at-a-distance [18–22] coupling. While recent attempts provide new and valuable insight, the overall dynamical picture remains far from being well understood. In particular, there have been few attempts at mapping coupled-laser dynamics in the parameter space of coupling strength versus detuning [6,12,13,23,24]. To help fill the gap, the goal of this paper is to provide a global understanding of coupled-cavity laser dynamics. By global we mean evolution of the entire dynamical picture encompassing (i) stationary points, (ii) periodic orbits, (iii) quasiperiodic oscillations, (iv) chaos, and (v) multistability, over an extensive range of key parameters. Of particular interest are the mutual connections between different types of dynamics, which can be understood via *organizing centers*. These higher-codimension bifurcation points are sources for various nonlinear phenomena. To perform our investigation, we use numerical tools from bifurcation theory on different dynamical regions in the plane of coupling strength versus cavity-length mismatch, for different values of the linewidth enhancement factor α and photon-to-population decay ratio. We consider the simple configuration of two end-to-end positioned lasers coupled with a common mirror of transmission T (Fig. 1). We choose a composite-cavity mode approach that has three benefits crucial to achieving our goal. First, the model is valid for arbitrary coupling-mirror transmission $T \in (0,1\rangle$. Second, it captures the nonlinear dependence of the composite-cavity modes on T and the cavity-length mismatch $\mathrm{d}L$. Third and most important, it allows straightforward bifurcation analysis using numerical bifurcation continuation techniques [43]. This is because the resulting multimode equations are ordinary differential equations for the fields of the lasing modes and population densities, that are coupled to the

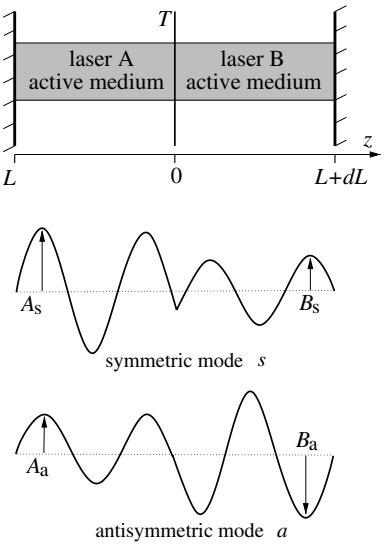

Fig. 1. (Top) Two lasers coupled with a common mirror of transmission T. (Bottom) A pair of passive composite-cavity modes for $dL > 0$.

Helmholtz equation for the passive composite-cavity modes [24].

Our previous work on the composite-cavity mode description for coupled lasers dealt with locking of class-A lasers, and with changes in the locking–unlocking mechanism under transition from class-A to class-B lasers [6,24,41]. We found that class-B lasers with significant refractive-index effects, e.g. semiconductor lasers, exhibit chaotic dynamics that interrupts the lockband in the plane of optical coupling strength versus cavity-length mismatch [24]. This paper presents a more detailed study of class-B lasers. (i) We expanded the parametric study by investigating dependences of the lockband on the linewidth enhancement factor α, and the ratio between the photon and population decay rates. In particular, we explained why a bistable and uninterrupted lockband at $\alpha = 0$ unfolds and develops a gap with increasing α. Also, we found that coupled lasers become more unstable at higher ratio between the photon and population decay rates. (ii) We performed a detailed study of bifurcations of periodic orbits, specifically their origins and mutual connections. We showed how the gap in the lockband is gradually occupied by instabilities and chaos with increasing α. (iii) We expanded on the counterintuitive effect of chaotic oscillations in microcavities with vanishing coupling strength [24]. In particular, we studied the effects of cavity length to show that chaos at ultra-weakly coupled microcavities is a mutation of chaos found for moderately coupled longer lasers.

Section 2 presents the equations for the time evolution of the slowly varying field amplitudes and phases associated with composite-cavity modes, and for population densities in both lasers. Also, it lists the parameter settings. Section 3 discusses nonlinearities imparted by the composite-cavity model, Section 4 deals with the symmetry properties of two-composite-mode coupled-cavity lasers. In Section 5 we present bifurcation diagrams and find that a bistable and uninterrupted lockband for the linewidth enhancement factor $\alpha = 0$ unfolds and develops a gap with increasing α. We describe how instabilities of periodic orbits, leading to complicated oscillations and chaos, fill this gap. We find that coupled-cavity lasers become more unstable at a higher photon-to-population decay ratio. Also, we explain why the region of complicated dynamics shifts in the direction of the origin in the $(T, dL/\lambda)$ plane with decreasing cavity-length.

2. Composite-cavity model

In the framework of semiclassical laser theory, the laser field for the coupled-laser structure from Fig. 1 is expanded in terms of the passive composite-cavity modes $u_n(z)$ [31]

$$\mathscr{E}(z,t) = \frac{1}{2}\sum_n \left[E_n(t)\mathrm{e}^{-\mathrm{i}\psi_n(t)}u_n(z) + \text{c.c.}\right]. \tag{1}$$

The slowly varying electric field amplitude $E_n(t)$, and phase $\psi_n(t)$ associated with the nth composite-cavity mode evolve according to [41]

$$\dot{E}_n = -\frac{\Gamma_E}{2}E_n + C_{nn}\Gamma\sum_k \left\{\frac{c}{n_b}\left[C^A_{kn}g^A + C^B_{kn}g^B\right]\times\cos(\psi_{kn}) + \frac{v}{n_b}\left[C^A_{kn}\delta n^A + C^B_{kn}\delta n^B\right]\sin(\psi_{kn})\right\}E_k, \tag{2}$$

$$\dot{\psi}_n = v_n + \dot{\phi}_n(t) = \Omega_n - C_{nn}\Gamma\sum_k \left\{\frac{v}{n_b}\left[C^A_{kn}\delta n^A + C^B_{kn}\delta n^B\right]\cos(\psi_{kn}) - \frac{c}{n_b}\left[C^A_{kn}g^A + C^B_{kn}g^B\right]\sin(\psi_{kn})\right\}\frac{E_k}{E_n}, \quad (3)$$

where c is the speed of light, $n_b = \sqrt{\epsilon_b}$ is the background refractive index assumed to be the same in both cavities, Γ_E is the composite-cavity mode decay rate, Γ is the composite-cavity mode confinement factor, Ω_n is the passive composite-cavity mode frequency, v_n is the optical frequency, $\phi_n(t)$ is the slowly varying phase of the nth composite-mode, and $\psi_{kn} = \psi_k - \psi_n$ is the phase difference between the lasing composite-cavity modes.

If the active medium polarization decays much faster than the population and photons (class-B laser approximation), electric field equations are coupled to the population density dynamics. The equation of motion for each laser population is [41]

$$\dot{N}_{A(B)} = \Lambda_{A(B)} - \Gamma_N N_{A(B)} - \frac{\epsilon_0\epsilon_b}{\hbar v}\sum_{m,n} C^{A(B)}_{nm}\frac{c}{n_b}g^{A(B)}\cos(\psi_{nm})E_mE_n, \quad (4)$$

where Λ_n is the excitation rate and Γ_N is the population decay rate. We assume an active-medium local-gain that is linear around the value N_{thr}

$$g^{A(B)} = g_{thr} + \xi(N_{A(B)} - N_{thr}),$$

where ξ is the differential gain. When the two cavities are uncoupled, the population density in individual lasers will equilibrate at N_{thr}. Expressions for N_{thr} and g_{thr} are given in Table 1. Furthermore, we use the linewidth enhancement factor α to quantify the population-induced local refractive-index-change

$$\delta n^{A(B)} = -\frac{c}{v}\alpha^{A(B)}\xi N_{A(B)}.$$

Passive composite-cavity modes $u_n(z)$ are determined from the Helmholtz equation [6]

$$\frac{d^2}{dz^2}u_n(z) = -\mu_0\epsilon_0\epsilon_b(z)\Omega_n^2 u_n(z), \quad (5)$$

where $\epsilon_b(z)$ is the position-dependent background dielectric constant of the coupled-cavity structure [6]. The solutions of Eq. (5) that satisfy appropriate boundary conditions become [6]

$$u_n(z) = A_n\sin\left[\Omega_n n_b(z+L)/c\right] \quad \text{for } -L \leqslant z \leqslant 0, \quad (6)$$

$$u_n(z) = B_n\sin\left[\Omega_n n_b(z-L-dL)/c\right] \quad \text{for } 0 \leqslant z \leqslant L + dL.$$

The field of a passive composite-cavity mode at the end mirrors can be in-phase or π out-of-phase (Fig. 1). Hence, composite modes are described as *symmetric* ($n = s_j$) and *antisymmetric* ($n = a_j$) [6], respectively.

Table 1
Definitions of dimensionless quantities and the local gain at threshold

Quantity	Physical context
$\tilde{t} = t/\Gamma_N$	Dimensionless time
$\tilde{N} = (N - N_{thr})/N_{thr}$	Dimensionless population density deviation from N_{thr}
$N_{thr} = N_{ts} + n_b\Gamma_E/(2c\Gamma\xi)$	Population density at threshold in a free-running laser
N_{ts}	Population density at transparency
$\tilde{E} = E/E_0$	Dimensionless electric field amplitude
$E_0 = \sqrt{2\hbar v\Gamma\Gamma_N N_{thr}/(\epsilon_0 n_b^2\Gamma_E)}$	Field of a free-running laser at twice threshold
$\tilde{\Omega}_k = \Omega_k/\Gamma_N$	Dimensionless passive composite-mode frequency
$\tilde{\Lambda}_{A(B)} = \Lambda_{A(B)}/\Lambda_{thr}$	Dimensionless excitation rate in cavity A(B)
$\Lambda_{thr} = \Gamma_N N_{thr}$	Threshold excitation rate in a free-running laser
$\gamma = \Gamma_E/(2\Gamma_N)$	Photon-to-population decay ratio
$\beta = 1 + 2c\Gamma\xi N_{ts}/(n_b\Gamma_E)$	Dimensionless gain coefficient
$g_{thr} = n_b\Gamma_E/(2c\Gamma)$	Local gain at N_{thr}
dL/λ	Dimensionless cavity-length mismatch
$\lambda = n_b L/10^3$	Approximate wavelength of a free-running laser

If an individual laser has $j = 1, \ldots, N$ lasing longitudinal modes, a double-cavity laser has $2N$ composite-cavity modes $n = a_1, s_1, \ldots, a_N, s_N$ [6]. In the problem of a multimode coupled-cavity laser, there are two types of spatial holes (Fig. 1): (i) *fine* holes spaced half-wavelength $\lambda/2$ apart that are burned by the standing wave, giving rise to a population grating as in a single-cavity laser [42], and (ii)*course* holes that are burned on the scale of the cavity length L because each composite-cavity mode has different amplitudes in the different cavities. The overall coupling between composite modes arises from fine and course spatial hole burning, and from spectral hole burning. While a population grating couples modes with different j, the course holes are responsible for the locking of the lasers. The general treatment that takes into account $2N$ composite modes, and population grating effects, is beyond the scope of the present investigation. Here, we consider two single-mode coupled lasers, e.g. microcavity or DFB lasers. There are then 2 composite-cavity modes u_a and u_s, and population grating effects are neglected.

The composite-cavity mode structure enters into the equations of motion (2)–(4) via the modal integrals $C_{nm} = C^A_{nm} + C^B_{nm}$. Using the orthogonality relation

$$\int_{-L}^{L+\mathrm{d}L} \mathrm{d}z \epsilon_b(z) u_n(z) u_m(z) = \mathcal{N}\delta_{nm}, \tag{7}$$

with the normalization constant $\mathcal{N} = n_b^2 L$ we get [41]

$$\begin{aligned} C^A_{nm} &= \frac{n_b^2}{\mathcal{N}} \int_{-L}^{0} \mathrm{d}z u_n(z) u_m(z) \\ &= \frac{1}{2L} A_n A_m \left(\frac{\sin[(k_n - k_m) n_b L]}{(k_n - k_m) n_b} - \frac{\sin[(k_n + k_m) n_b L]}{(k_n + k_m) n_b} \right), \end{aligned} \tag{8}$$

$$\begin{aligned} C^B_{nm} &= \frac{n_b^2}{\mathcal{N}} \int_{0}^{L+\mathrm{d}L} \mathrm{d}z u_n(z) u_m(z) \\ &= \frac{1}{2L} B_n B_m \left(\frac{\sin[(k_n - k_m) n_b (L + \mathrm{d}L)]}{(k_n - k_m) n_b} \right. \\ &\quad \left. - \frac{\sin[(k_n + k_m) n_b (L + \mathrm{d}L)]}{(k_n + k_m) n_b} \right). \end{aligned} \tag{9}$$

These integrals describe the overlap of the composite-cavity modes with the active media. Also, they provide information about the composite-mode coupling which is due to two physical effects [37]. One, associated with the composite-mode structure and proportional to $\sum_{i=A,B} C^i_{nn} C^i_{mm}$, is the *spatial hole burning*. The other, associated with the active medium dynamics, is *population pulsation* at the beat note frequency $\dot{\psi}_{nm}$. The latter is proportional to $\sum_{i=A,B} (C^i_{nm})^2$ and becomes significant when $\Gamma_N \gtrsim |\nu_m - \nu_n|$ [41].

For convenience, we transform the equations of motion into a dimensionless form. Using the dimensionless quantities given in Table 1 we rewrite (2)–(4) to arrive at our working equations

$$\begin{aligned} \dot{\tilde{E}}_n &= -\gamma \tilde{E}_n + C_{nn}\gamma \sum_k \left\{ \left[C^A_{kn}(1 + \beta \tilde{N}^A) \right. \right. \\ &\quad \left. + C^B_{kn}(1 + \beta \tilde{N}^B) \right] \cos(\psi_{kn}) - \beta \left[C^A_{kn} \alpha^A (1 + \tilde{N}^A) \right. \\ &\quad \left. \left. + C^B_{kn} \alpha^B (1 + \tilde{N}^B) \right] \sin(\psi_{kn}) \right\} \tilde{E}_k, \end{aligned} \tag{10}$$

$$\begin{aligned} \dot{\psi}_n &= \tilde{\Omega}_n + C_{nn}\gamma \sum_k \left\{ \beta \left[C^A_{kn} \alpha^A (1 + \tilde{N}^A) \right. \right. \\ &\quad \left. + C^B_{kn} \alpha^B (1 + \tilde{N}^B) \right] \cos(\psi_{kn}) + \left[C^A_{kn}(1 + \beta \tilde{N}^A) \right. \\ &\quad \left. \left. + C^B_{kn}(1 + \beta \tilde{N}^B) \right] \sin(\psi_{kn}) \right\} \frac{\tilde{E}_k}{\tilde{E}_n}, \end{aligned} \tag{11}$$

$$\begin{aligned} \dot{\tilde{N}}_{A(B)} &= \tilde{\Lambda}_{A(B)} - (\tilde{N}_{A(B)} + 1) - \sum_{m,n} C^{A(B)}_{nm} (1 + \beta \tilde{N}^{A(B)}) \\ &\quad \times \cos(\psi_{nm}) \tilde{E}_m \tilde{E}_n, \end{aligned} \tag{12}$$

with two types of parameters. The coupling parameters namely, the coupling-mirror transmission T and the cavity-length mismatch $\mathrm{d}L$, appear implicitly through the modal integrals $C^{A(B)}_{nm}$. Also, they determine the passive composite-cavity-mode frequencies $\tilde{\Omega}_n$. The number of laser parameters characterizing active media, external excitation, and decay of photons, has been reduced to six effective parameters. These are the linewidth enhancement factors $\alpha^{A(B)}$, dimensionless gain coefficient β, dimensionless excitation rates $\tilde{\Lambda}_{A(B)}$, and the ratio between the photon and population decay rates γ.

To describe quantum-well semiconductor lasers, such as distributed feedback lasers, we chose

the material parameters to be $n_b = 3.4$, $\xi = 2.5 \times 10^{-20}$ m^2, $\Gamma = 0.1$, and $N_{ts} = 2.0 \times 10^{24}$ m^{-3} [44, p. 96]. The lasers are biased at twice threshold $\tilde{\Lambda}_{A(B)} = 2$. The linewidth enhancement factors are assumed to be identical in both lasers, and we consider α ranging from $\alpha = 0$ to $\alpha = 3$. Furthermore, we use two combinations of the photon and population decay rates $\Gamma_E = 10^{11}$ s^{-1}, $\Gamma_N = 5 \times 10^9$ s^{-1}, and $\Gamma_E = 2 \times 10^{11}$ s^{-1}, $\Gamma_N = 10^9$ s^{-1}, to study effects of different $\gamma = \Gamma_E/(2\Gamma_N)$. For most of the calculations we assume $L = 280$ μm. In Section 5.4 L is decreased to 2.8 μm.

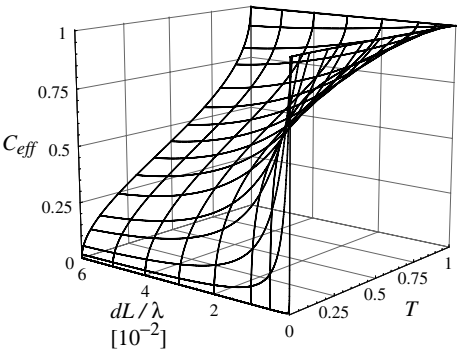

Fig. 2. Effective coupling between lasers $C_{\text{eff}} \equiv A_a/B_a$ as a function of the coupling parameters T and dL/λ.

3. Model nonlinearities

In this section we describe the two sources of nonlinearities in the composite-cavity model: the active medium dynamics and the optical coupling between resonators. In our approach, the laser problem is separated in active and passive parts [Eq. (1)]. As a consequence of this approximation, active medium nonlinearities are treated through the electric field and population equations of motion, and the coupled resonator nonlinearities are treated through Helmholtz equation and associated boundary conditions.

Population dynamics, when coupled to electric field variations, bring in an extra degree of freedom, so that a single-mode class-B laser becomes a nonlinear oscillator. Away from threshold, it exhibits damped periodic oscillation at the characteristic (relaxation oscillation) frequency

$$\omega_R \simeq \sqrt{\frac{2c\Gamma\xi}{n_b}(\Lambda - \Lambda_{thr})} = \Gamma_N \sqrt{2\gamma\beta(\tilde{\Lambda} - 1)}. \quad (13)$$

A strong enough driving force, e.g. pump modulation or externally injected light detuned at a frequency near ω_R, is known to undamp relaxation oscillation and possibly induce instabilities and chaos. In a multimode laser, more nonlinearities appear due to the mode interaction via the active medium. As a consequence of this interaction, population is modulated at the beat note frequency $\dot{\psi}_{nm}$ as represented by the off-diagonal ($n \neq m$) terms in Eqs. (4) and (12). This population pulsation interacts with mode n to produce oscillation at the frequency of mode m. A result is an additional cross-saturation of mode m, being a part of spectral hole burning.

Nonlinearities due to the optical coupling between resonators manifest under variation of the coupling parameters T and dL. Let us define the effective coupling between lasers as the ratio of the amplitudes of a single composite-cavity mode in the two cavities, i.e. $C_{\text{eff}} \equiv A_a/B_a \simeq -B_s/A_s$, where $C_{\text{eff}} \in \langle 0,1 \rangle$. While T describes properties of the coupling mirror in free space, the effective coupling describes how changes in the field in one cavity influence the field in the other cavity. To examine nonlinearities in the effective coupling, we plot in Fig. 2 C_{eff} as a function of T and dL/λ. The discussion is for $dL > 0$. For $dL < 0$ we simply interchange 'symmetric' and 'antisymmetric'. When $A_a/B_a \sim 0$, the two composite-cavity modes are basically the modes of individual lasers. The symmetric mode resides primarily in laser A and the antisymmetric mode resides primarily in laser B. For equally long cavities, the cavity resonance results in maximum effective coupling, $A_a/B_a = 1$, regardless of the coupling-mirror transmission T. The lower the value of T, the sharper is the decrease in the effective coupling as a function of dL. Eventually, in the limit $T \to 0$ the effective coupling becomes singular at $dL = 0$. These dependencies do not change with L as long as $L \gg \lambda$. Note that comparable amplitudes $A_a \sim A_s$ and $|B_a| \sim |B_s|$ mark the parameter settings where the composite-cavity modes are strongly coupled due to spatial hole burning.

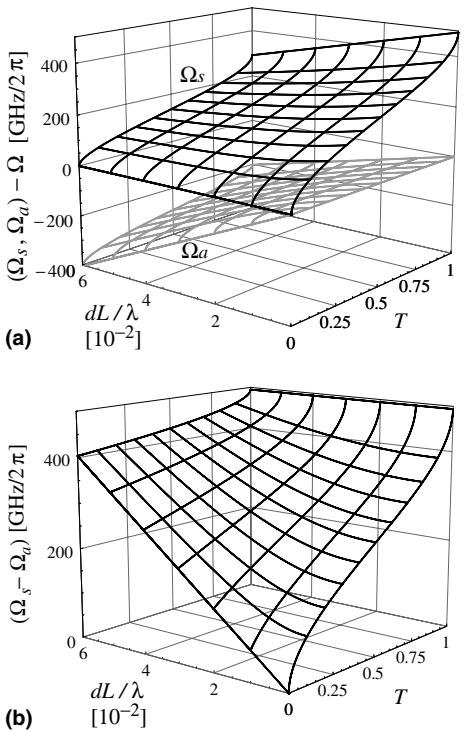

Fig. 3. (a) Passive composite-cavity mode frequencies and (b) composite-cavity mode detuning as a function of the coupling parameters T and $\mathrm{d}L/\lambda$. Ω is a passive-mode frequency of a single resonator of length L.

Nonlinearities of the passive composite-mode frequencies, and their detuning, are shown in Fig. 3. Frequencies of isolated resonators ($T = 0$) are determined by the resonances of separate resonators [Fig. 3(a)] such that for $\mathrm{d}L \sim \lambda$ and $\lambda \ll L$ we have $(\Omega_\mathrm{s} - \Omega_\mathrm{a}) \simeq \Omega_n \,\mathrm{d}L/L$ [Fig. 3(b)]. With no coupling mirror ($T = 1$) the composite-cavity modes become the modes of a single cavity of length $2L + \mathrm{d}L$. They differ by half of the wavelength and $(\Omega_\mathrm{s} - \Omega_\mathrm{a}) \simeq \pi c/(2Ln_\mathrm{b})$. For $0 < T < 1$, the passive composite-cavity mode frequencies, and their detuning, are nonlinear functions of T and $\mathrm{d}L$.

The interplay between nonlinearities due to the active medium dynamics and those associated with the optical coupling manifests, under appropriate conditions, in rich dynamical behavior described in Section 5.

4. Symmetry properties

In this section, we discuss symmetries in the presence of two composite-cavity modes $n(m) = a,s$. Because each composite mode has different spatial overlap with the active media there is no perfect symmetry in the system of coupled-cavity lasers. However, for long (compared to the wavelength) cavities this difference is small enough so that the system appears to have some symmetries. If $L \gg \lambda$ (this works well already when $L \sim 10\lambda$), we have that $C^A_{nn} \simeq C^B_{mm}$, and $C^A_{nm} \simeq -C^B_{nm}$ for $n \neq m$. Furthermore, if $L \gg \lambda$ and $\mathrm{d}L \sim \lambda$ we have that $(C^A_{nn}, \mathrm{d}L) \to (C^B_{nn}, -\mathrm{d}L)$.

One consequence of the above relations is the reflection symmetry $(\psi_{mn}, N^A, N^B, \alpha^A, \alpha^B, \Lambda_A, \Lambda_B, \mathrm{d}L) \to (\psi_{mn} \pm \pi, N^B, N^A, \alpha^B, \alpha^A, \Lambda_B, \Lambda_A, -\mathrm{d}L)$. Hence, the bifurcation diagram in the $(T, \mathrm{d}L)$ plane can be symmetric with respect to the change $\mathrm{d}L \to -\mathrm{d}L$, provided that both lasers are equally excited ($\Lambda_A = \Lambda_B$) and experience the same refractive-index-effect ($\alpha^A = \alpha^B$).

Another consequence is the symmetry in stationary points of (steady state solutions to) in the $\{\mathrm{E_a}, \mathrm{E_s}, \psi_\mathrm{as}, \mathrm{N_A}, \mathrm{N_B}\}$ phase space. Under the assumption of equally biased lasers, equal losses for both composite-modes, and no refractive-index-effect ($\alpha^A = \alpha^B = 0$), we notice that if $\{E^0_\mathrm{a}, E^0_\mathrm{s}, \psi^0_\mathrm{sa}, N^0_A, N^0_B\}$ is a stationary point, then $\{E^0_\mathrm{s}, E^0_\mathrm{a}, \psi^0_\mathrm{sa} \pm \pi, N^0_B, N^0_A\}$ is a stationary point too. Each of the two points may sometimes be associated with lasing at a single composite-cavity mode. Whether both of them are stable at the same time depends on the competition between the composite-cavity modes. Strong competition results in bistability between these two stationary points [37].

5. Bifurcations and resulting dynamics

In the coupled-cavity laser, dynamics arise from the interaction of active media with the composite-mode beat note, from frequency locking of the composite-cavity modes, and from competition between the composite-cavity modes. Instabilities appear when two conditions are satisfied simultaneously. (i) The intermode frequency has

to be near the relaxation oscillation frequency $|\nu_n - \nu_m| \sim \omega_R$ providing strong coupling of the lasing field and active media. (ii) A strong coupling between the lasing modes has to be present. The latter arises from spatial hole burning due to significant spatial overlap of the composite-cavity modes, and from population pulsation [37]. Solutions to the set of Eqs. (5) and (10)–(12) can be very complicated, even chaotic. While physical intuition is important to identify the underlying nonlinearities, it does not always provide a satisfactory explanation for the resulting dynamics. In such situations, bifurcation analysis is the tool of choice.

In this section, we present the results as bifurcation diagrams in the $(T,\mathrm{d}L/\lambda)$ plane. Furthermore, we study the dependence of the dynamics on T and $\mathrm{d}L/\lambda$ for different but fixed values of α, and for different but fixed values of $\gamma = \Gamma_E/2\Gamma_N$. As T or $\mathrm{d}L/\lambda$ are changed continuously, qualitative changes called bifurcations [45] appear in the phase portraits of Eqs. (10)–(12). Once detected, bifurcations of stable objects (called supercritical) as well as bifurcations of unstable objects (called subcritical and needed for consistent dynamical picture as they sometimes produce stable states) can be continued in two parameters [43]. As a result, the $(T,\mathrm{d}L/\lambda)$ plane is divided by bifurcation curves into regions of different dynamics, forming a bifurcation diagram.

Our analysis starts with bifurcations of stationary points. Next, we identify organizing centers giving rise to bifurcations of periodic orbits. Then, bifurcations of periodic orbits are studied to uncover regions of complicated dynamics and chaos. All bifurcation curves are obtained using Eqs. (10)–(12) for a pair of composite-cavity modes, called symmetric ($n = s$) and antisymmetric ($n = a$). The composite modes are determined from Eq. (5) and appropriate boundary conditions [6].

5.1. Lockband

A lockband is the region in the $(T,\mathrm{d}L/\lambda)$ parameter space where both lasers emit light of constant intensities and the same frequency. This can be achieved in two ways: through phase locking of the composite-cavity modes or when both lasers operate at a single composite-cavity mode. A stable stationary point in the $\{E_a,E_s,\psi_{as},N_A,N_B\}$ phase space corresponds to locking. A stationary point may collide with another stationary point to disappear in saddle-node bifurcation. Also, it may change stability while giving rise to a periodic orbit in Hopf bifurcation. In Fig. 4, we plot saddle-node bifurcation curves S in blue and Hopf bifurcation curves H in red. Furthermore, for bifurcations of stationary points we distinguish between their supercritical (solid curves in darker tone) and subcritical (dashed curves in lighter tone) parts. When $\alpha = 0$ the lockband, that is the region in the $(T,\mathrm{d}L/\lambda)$ plane where both lasers operate at the same frequency, is bounded by supercritical parts of S and H.

Let us first focus on Fig. 4(a) for $\alpha = 0$, $\Gamma_E = 10^{11}\ \mathrm{s}^{-1}$ and $\Gamma_N = 5\times 10^9\ \mathrm{s}^{-1}$ ($\gamma = 10$). The two composite-cavity modes are in strong competition causing bistability inside the lockband. Saddle-node and Hopf bifurcations associated with both stationary points are tangent at $T \approx 0.027$, at four locations, where they change from supercritical to subcritical [Fig. 4(a)]. The tangency points G are the codimension-two saddle-node-Hopf points [45, Section 8.5]. Starting inside the lockband and increasing $|\mathrm{d}L/\lambda|$, the locking is lost either via saddle-node bifurcation ($T < 0.027$) or via Hopf bifurcation ($T > 0.027$). Although there are two different bifurcations responsible for the locking–unlocking transition, one can distinguish three different locking–unlocking mechanisms.

For $T < 0.027$ each of the two bifurcating stable stationary points has contributions from both composite modes [top panel of Fig. 4(a)]. Inside the lockband, $\dot{\psi}_{sa} = 0$ and the composite modes are phase locked. Here, frequency separation of composite-cavity modes is small, and the locking–unlocking transition is due to phase locking of the two composite modes. In the $\{E_a,\ E_s,\ \psi_{sa},\ N_A,\ N_B\}$ space, this is represented by two saddle-node-of-stationary-point bifurcations taking place on a single periodic orbit. Such a scenario was recognized in [41] as typical for weakly coupled class-B lasers.

For $T \gtrsim 0.15$, each of the two bifurcating stable stationary points has a large contribution from one composite mode, and a vanishing contribution

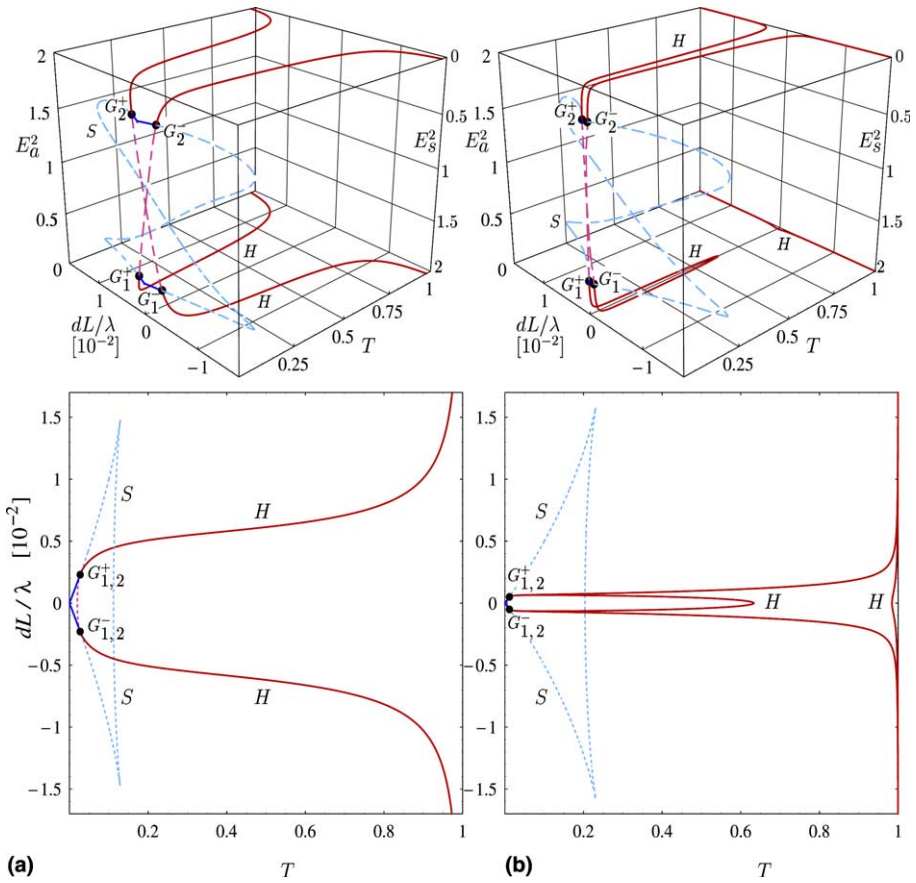

Fig. 4. Bifurcations of stationary points shown as (top) a three-dimensional bifurcation diagram in the $(T,\mathrm{d}L/\lambda,E^2_{a(s)})$ space and (bottom) a projection onto the $(T,\mathrm{d}L/\lambda)$ parameter plane. Supercritical parts of saddle-node bifurcation S (blue) and Hopf bifurcation curve H (red) bound the lockband and are plotted as solid curves, subcritical parts of S and H are plotted as dashed curves. S and H are tangent and change from supercritical to subcritical at codimension-two saddle-node-Hopf points G. The linewidth enhancement factor $\alpha = 0$, $L = 280$ μm, (a) $(\Gamma_E,\Gamma_N) = (10^{11}\ \mathrm{s}^{-1}, 5\times10^{9}\ \mathrm{s}^{-1})$, and (b) $(\Gamma_E,\Gamma_N) = (2\times10^{11}\ \mathrm{s}^{-1}, 10^{9}\ \mathrm{s}^{-1})$.

from the other composite mode. Inside the lockband, each of the two points correspond to lasing at a single composite-cavity mode [top panel of Fig. 4(a)]. Here, because of a large separation of the composite-mode frequencies, their phases are not important in the locking–unlocking transition. Locking arises from strong competition, due to cross-saturation, between the two composite modes. Unlocked operation is represented by a single (no bistability) stable periodic orbit [24] and involves both composite modes. The intensity of each mode slowly oscillates at the beat note frequency $\dot{\psi}_{\mathrm{sa}}$ due to population pulsation, and no instabilities appear with increasing $|\mathrm{d}L/\lambda|$. Such a scenario is typical for class-A lasers and involves saddle-node-of-periodic-orbit bifurcation [41]; see also Figs. 6(a) and 8(a) ahead.

The most interesting region lies in between the two, near G points, where neither the frequency locking description nor the competing mode description is valid. This is where the beatnote frequency $\dot{\psi}_{\mathrm{sa}}$ comes close to the relaxation oscillation frequency. For $0.027 < T \lesssim 0.1$, starting within the lockband, locking is lost via undamping of the relaxation oscillation. The two stable stationary points turn unstable and each of them gives rise to one stable periodic orbit. Outside the lockband and near G, these two periodic orbits

(bistability in unlocked operation) encounter instabilities leading to complicated dynamics and chaos [46]. It is interesting to note that, as T increases, the transition between the first and the second locking mechanism is clear cut, indicated by G. On the other hand, the transition between the second and the third locking mechanism happens continuously and involves saddle-node-of-periodic-orbit bifurcation.

As a consequence of symmetry and strong composite-mode competition, there can be bistability between the stable stationary points. Bifurcations associated with different stationary points may fully overlap as can be seen from the projection of the bifurcation diagram onto the (T,dL/λ) plane in the bottom panel of Fig. 4(a). Henceforth, we use the term *degenerate* to describe two overlapping bifurcations that appear as a single curve or point in the (T,dL/λ) plane. How can this degeneracy be removed?

5.1.1. Effect of γ

One straightforward way is to decrease competition between composite modes via decreasing population pulsation contribution to cross-saturation. To this end we decrease Γ_N to 10^9 s^{-1}; we also increase Γ_E to 2×10^{11} s^{-1} to obtain $\gamma = 100$. As shown in Fig. 4(b) bifurcations associated with different stationary points no longer fully overlap and a region of weak competition emerges for $0.65 \lesssim T \lesssim 0.98$. There, the symmetric mode experiences negative effective gain and the antisymmetric mode inhibits its oscillations. Furthermore, the lockband gets narrower than for $\gamma = 10$ [41]. A decrease in the relaxation oscillation frequency causes the G points to shift towards the origin of the (T,dL/λ) plane. However, the degeneracy of $G^{+}_{1(2)}$ and $G^{-}_{1(2)}$ remains.

5.1.2. Effect of α

While the majority of solid-state lasers and most popular gas lasers, such as CO_2 lasers, usually have $\alpha \sim 0$, typical semiconductor lasers are characterized by α varying from 1 to 4 [44]. To explore dynamics of different types of lasers and to understand how qualitative differences in the behavior of different lasers come about, we focus our attention on evolution of the lockband with increasing α. The two lockbands in Fig. 5, associated with the two stable stationary points, are distinguished with left-inclined and right-inclined patterns, respectively. Let us recall that bifurcation theory predicts four different types of a saddle-node-Hopf point, and all four G points from Fig. 5(a) are of type IV according to notation from [45].

Increasing α above zero unfolds the otherwise degenerate bifurcation diagram [Fig. 5(a)] so that for nonzero α neither bifurcation curves nor $G_1^{+(-)}$ and $G_2^{+(-)}$ fully overlap [Fig. 5(b)]. One lockband, associated with G_1^{+} and G_1^{-}, expands along the dL/λ axis and moves in the direction of lower values of T. The other lockband, associated with G_2^{+} and G_2^{-}, moves together with G_2^{+} and G_2^{-} in the direction of higher values of T. Furthermore, lockband associated with G_1^{+} and G_1^{-} is no longer bounded by the entirely supercritical Hopf bifurcation curve. Codimension-two generalized-Hopf bifurcation points H_g appear where the Hopf curve changes from supercritical to subcritical. Throughout the range of α under consideration, the type of G_2^{+} and G_2^{-} remains unchanged. On the other hand, G_1^{+} and G_1^{-} change from type IV to type III (according to notation from [45]) at $\alpha \simeq 0.5$. The bifurcation diagram in Fig. 5(c) shows that H curve has a cusp at G_1^{+} and G_1^{-} which makes this a very special point – bifurcation of codimension at least three. During the change in the type of G_1^{+} and G_1^{-}, the two branches of H, one supercritical and the other subcritical, connecting at $G_1^{+(-)}$ flip. This has important consequences to where the chaotic dynamics associated with $G_1^{+(-)}$ appear; see the next section for explanation. Increasing α further, results in less overlap between the two lockbands to the point where they no longer coalesce [Fig. 5(d)]. At $\alpha = 1$ the two lockbands are well separated and a gap appears where couple-cavity lasers never lock. This gap increases with further increase of α [Fig. 5(e)] so that for $\alpha = 3$ there are two distinct lockbands [Fig. 5(f)]. One at low coupling-mirror transmissions $0 < T < 0.01$ and the other at relatively high coupling-mirror transmissions $0.45 < T < 1$. Also, generalized Hopf points H_g are gone and both lockbands are again bounded by the entirely supercritical parts of S and H.

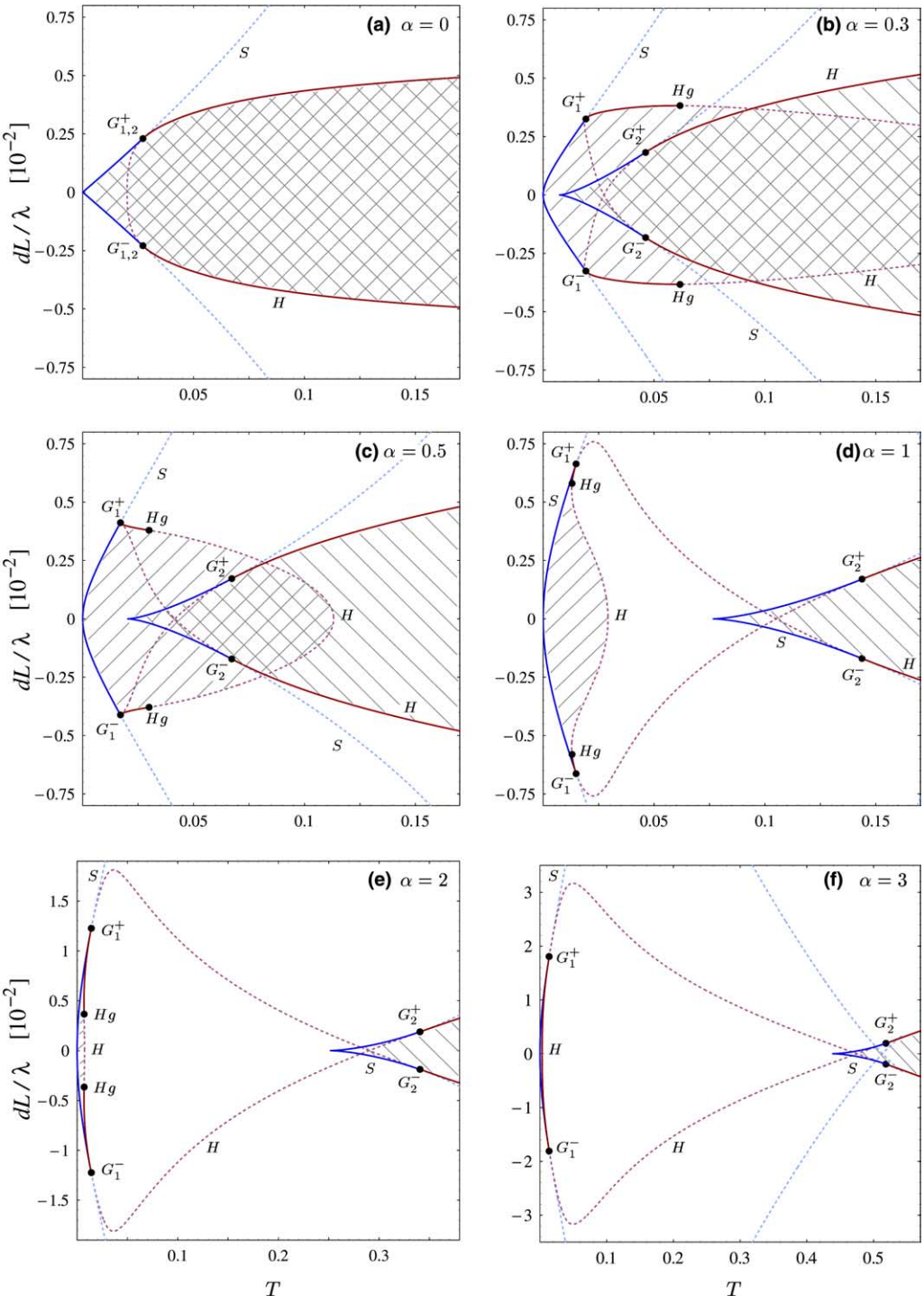

Fig. 5. Lockband in the (T,dL/λ) plane for different values of the linewidth enhancement factor α. Saddle-node bifurcations S are in blue, Hopf bifurcations H are in red, right-inclined and left-inclined patterns denote the two lockbands, respectively. S and H are tangent and change from supercritical to subcritical at codimension-two saddle-node-Hopf points G. H also changes from supercritical to subcritical at generalized Hopf points H_g. For this figure $L = 280$ μm, $\Gamma_E = 10^{11}$ s^{-1}, and $\Gamma_N = 5 \times 10^9$ s^{-1}.

The changes in the lockband due to α can be understood intuitively. In a free-running laser, population density equilibrates at N_{thr}. When two lasers of different length and $\alpha = 0$ are coupled, there are two possibilities for stable stationary points (locking). One, the lockband associated with $G_1^{+(-)}$, where population equilibrates below (above) N_{thr} in the shorter (longer) cavity. And the other, the lockband associated with $G_2^{+(-)}$, where population equilibrates below (above) N_{thr} in the longer (shorter) cavity. If $\alpha = 0$ the lasing frequency of each laser is affected by the field of the other laser but not by different population levels due to the coupling. However, when α increases from zero, the lasing frequencies in the cavities shift accordingly to the population levels and the lockbands change. The lockband associated with $G_2^{+(-)}$ moves in the direction of higher T because the lasing frequencies in the two cavities shift apart so that higher coupling is required to achieve locking. The lockband associated with $G_1^{+(-)}$ expands in the direction of $\mathrm{d}L/\lambda$ because the lasing frequencies in the two cavities shift towards each other so that locking can be achieved for lower coupling. Furthermore, this lockband disappears from the region of high T. In terms of the composite-cavity modes, the linewidth enhancement factor appears to decrease composite-mode competition so that bistability is no longer possible.

5.2. Bifurcations of periodic orbits

The next question concerns dynamics for parameter settings within the gap between the two lockbands. In a coupled-cavity laser, periodic orbits emerge along Hopf bifurcation curves H, along curves S of global saddle-node bifurcation (homoclinic bifurcation to a nonhyperbolic equilibrium [45]), and along homoclinic bifurcation curves h. In homoclinic bifurcation (plotted in dotted black) the period of the bifurcating orbit goes to infinity as the orbit hits the saddle stationary point. Furthermore, periodic orbits encounter instabilities as the parameters are varied. In period doubling bifurcation PD (plotted in green) period-one orbit gives rise to period-two orbit of twice the period of period-one orbit. In torus (Neimark–Sacker) bifurcation T (plotted in solid black), extra frequency appears in the system as the periodic orbit changes stability and gives rise to a 2-torus (two-dimensional torus). In saddle-node-of-periodic-orbit bifurcation SL (plotted in brown) two periodic orbits merge and disappear.

Bifurcation theory provides the rules on *where* and *how* different bifurcations of periodic orbits are associated with bifurcations of stationary points and with themselves [45]. Therefore, they do not have to be blindly searched for. The key points in a two-dimensional bifurcation diagram are codimension-two points where two or more bifurcation curves merge. Some of these points, also called organizing centers for the dynamics, often require existence of additional bifurcation curves that can be found near them. We already identified two types of codimension-two bifurcations namely, saddle-node-Hopf points G and generalized Hopf points H_{g}. Both are sources of bifurcations of periodic orbits and hence, the starting point for the further analysis.

Since the bifurcation diagram in the $(T,\mathrm{d}L/\lambda)$ plane depends strongly on α as well as on the photon-to-population decay ratio γ, we present series of bifurcation diagrams with varying α for the two settings of $\gamma = 10$ and 100. Note that for bifurcations of periodic orbits we do not distinguish between supercritical and subcritical parts.

5.2.1. Small photon-to-population decay ratio $\gamma = 10$

In Fig. 6, we show bifurcations of stationary points and periodic orbits for $\Gamma_E = 10^{11}\ \mathrm{s}^{-1}$ and $\Gamma_N = 5 \times 10^9\ \mathrm{s}^{-1}$. As expected from general theory [45], there is a torus bifurcation curve T emerging from each G point [Fig. 6(a)]. Only two of four T curves are visible due to the degeneracy. These torus curves correspond to competition between the relaxation oscillation frequency and the intermode frequency. They are associated with resonance tongue structure (not shown here) and denote the onset of either quasiperiodic (parameter settings between the tongues) or periodic (parameter settings within a resonance tongue) oscillations when the solid black T curves are crossed from the right to the left [47]. Also, they signal appearance of chaos via break-up of 2-torus when the

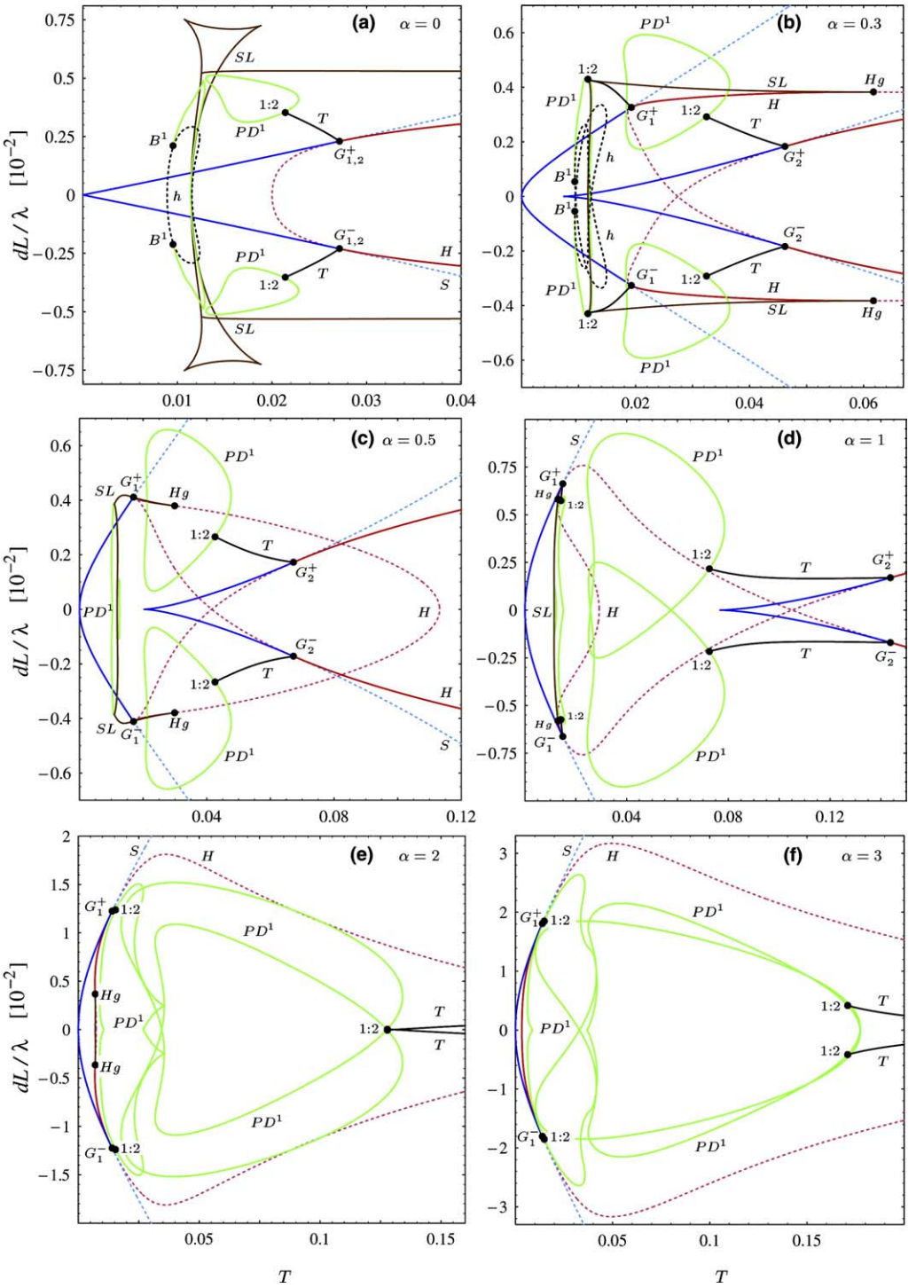

Fig. 6. Bifurcation diagram in the $(T,\mathrm{d}L/\lambda)$ plane for different values of the linewidth enhancement factor α. Saddle-node bifurcation curves are in blue, Hopf bifurcation curves are in red, period-doubling bifurcation curves *PD* are in green, saddle-node-of-periodic-orbit bifurcation curves *SL* are in brown, torus bifurcation curves *T* are in solid black, and homoclinic bifurcation curves *h* are in dotted black. We use $L = 280$ μm, $\Gamma_E = 10^{11}$ s^{-1}, and $\Gamma_N = 5\times10^9$ s^{-1}.

resonance tongues start to overlap. The T curves terminate at so called 1:2 resonance points [45, Section 9.5.3] where they connect to period-doubling curves PD^1. The PD^1 curves are the first steps in the infinite period-doubling cascade to chaos [48]. The secondary period-doubling curves $PD^{n>1}$ may be arranged in nested or unnested islands of period-doublings [49]. In either case, period-doubling islands are associated with chaotic dynamics. One of the period-doubling curves from Fig. 6(a) does not form a closed loop but terminates at two homoclinic-doubling bifurcation points B^1 [50]. Furthermore, there is a non-degenerate saddle-node-of-periodic-orbit curve SL where one of the two stable periodic orbits, born along the degenerate H curve, disappears. The overall dynamical picture for $\alpha = 0$ consist of the bistable lockband and complicated, sometimes chaotic, dynamics found outside of the lockband and near G points.

When α is increased from zero [Fig. 6(b)], the degeneracy unfolds and one clearly sees four torus curves connecting to period-doubling curves at four 1:2 resonance points. Interestingly, regions of the complicated dynamics associated with $G_2^{+(-)}$ start to overlap with the lockband associated with $G_1^{+(-)}$. There, depending on initial conditions, coupled lasers may either be locked or exhibit complicated oscillations. At the generalized Hopf points H_g, SL attaches to the supercritical branches of H emerging from G_1^+ and G_1^-, causing the H curves to change from supercritical to subcritical. Stable periodic orbits born along these supercritical branches of H disappear at SL.

Increasing α further results in no qualitative changes to saddle-node-Hopf points $G_2^{+(-)}$ nor associated torus and period-doubling bifurcations. As the gap between the two lockbands appears [Fig. 6(c)–(f)], the $G_2^{+(-)}$ points move in the direction of higher values of T. Concurrently, the two torus curves T emerging from G_2^+ and G_2^- are dragged behind, causing the two attached period-doubling cascades to shift into the gap between the two lockbands. On the other hand, a number of qualitative changes take place near $G_1^{+(-)}$. For $\alpha \lesssim 0.5$, bifurcations of periodic orbits emerging from $G_1^{+(-)}$ evolve in the direction of increasing $|\mathrm{d}L/\lambda|$. Near $\alpha = 0.5$, the type of G_1^+ and G_1^- changes. The two branches of H, one supercritical and the other subcritical, connecting at $G_1^{+(-)}$ flip and so do the associated bifurcations of periodic orbits. The details near G_1^+ are shown in Fig. 7. Close to $\alpha \simeq 0.5$ a new SL curve appears that connects to H at the two H_g points, and has a cusp near $(T,\mathrm{d}L/\lambda) = (0.016,0.4125)$ [Fig. 7(b)]. The torus curve T detaches from G_1^+ and attaches near the cusp of this new SL curve at 1:1 resonance [45, Section 9.5.2]. At $\alpha = 1$ [Fig. 7(c)] the extra SL curve is gone. The torus curve T attaches again to G_1^+ but is flipped from above to below the S curve [Fig. 7(c) and (d)]. As a consequence, starting at $\alpha \simeq 1$ [Fig. 6(d)], the two torus curves T emerging from G_1^+ and G_1^-, and the attached period-doubling curves PD^1, start filling the gap between the two lockbands [Fig. 6(d)–(f)]. For clarity, only parts of the PD^1 curves associated with G_1^+ and G_1^- are plotted in Fig. 6(b)–(f).

5.2.2. Large photon-to-population decay ratio $\gamma = 100$

In Fig. 8, we show bifurcations of stationary points and periodic orbits for $\Gamma_E = 2 \times 10^{11}$ s^{-1} and $\Gamma_N = 10^9$ s^{-1}. Increasing the ratio between the composite-cavity mode Γ_E and the population Γ_N decay rates makes coupled lasers more unstable. The lockband narrows. The system becomes much more sensitive to α. New bifurcations appear that lead to complicated dynamics not observed at lower γ.

The main difference between Fig. 8(a) and 6(a) for $\alpha = 0$ is the absence of homoclinic-doubling points B_1 and the appearance of TS points. At TS saddle-node-of-periodic-orbit curve SL is tangent to torus curve T. The complete bifurcation structure near TS points is not understood yet and such points have not been studied in laser systems before.

The degenerate bifurcation diagram from Fig. 8(a) unfolds with increasing α [Fig. 8(b)] in a similar fashion as for $\gamma = 10$. The type of $G_2^{+(-)}$ remains unchanged while the type of $G_1^{+(-)}$ changes. The saddle-node-of-periodic-orbit curve SL attaches to the H curve at two generalized Hopf points H_g. Bifurcations of periodic orbits associated with $G_1^{+(-)}$ and $G_2^{+(-)}$ fill the gap between the two lockbands. However, all these

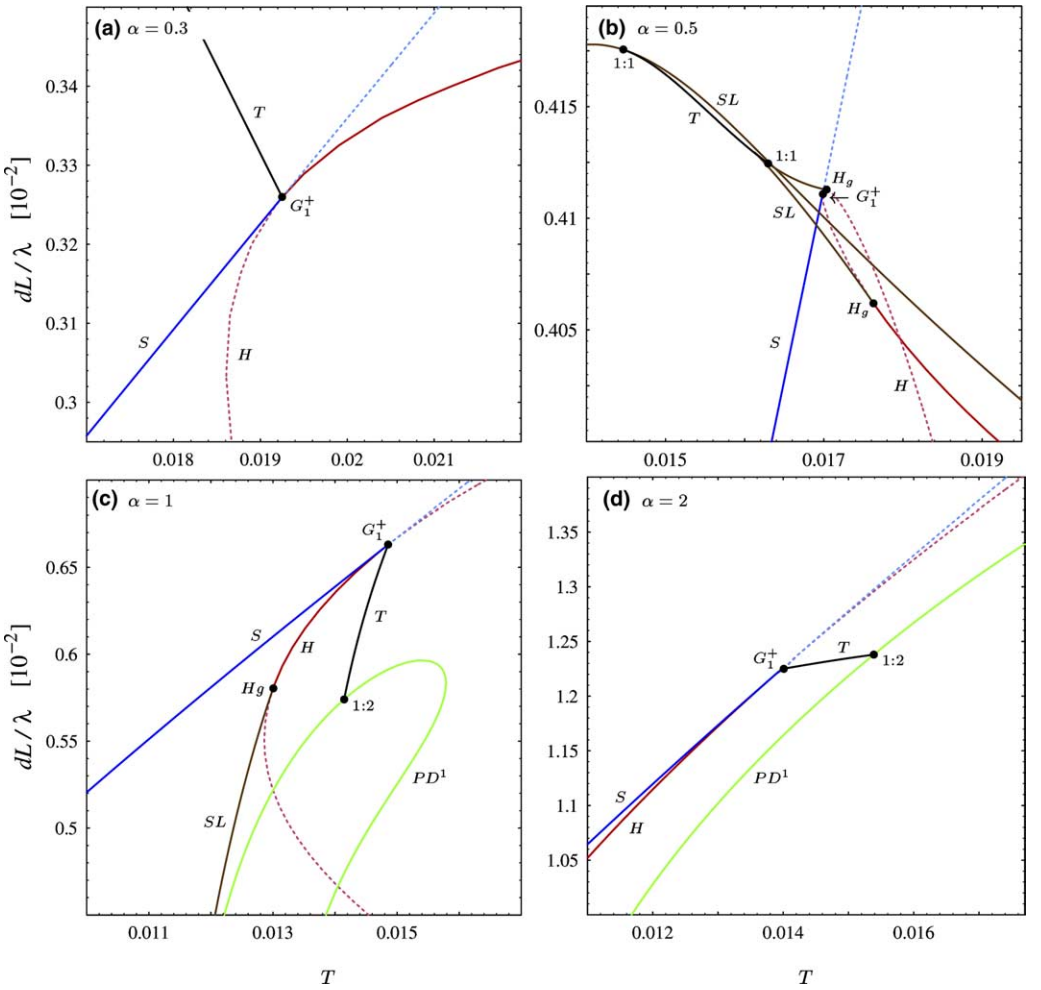

Fig. 7. Bifurcation diagram near saddle-node-Hopf point G_1^+ for different values of the linewidth enhancement factor α. We use $L = 280$ μm, $\Gamma_E = 10^{11}$ s^{-1}, $\Gamma_N = 5 \times 10^9$ s^{-1}, and the color coding is as in Fig. 6.

changes take place at much lower values of α. The gap between the two lockbands appears for $\alpha \sim 0.2$ and the change in the type of $G_1^{+(-)}$ takes place for $\alpha = 0.225$ [Fig. 8(c)]. As a consequence, already for $\alpha = 0.5$ a large gap between the two lockbands is filled with complicated dynamics due to the torus bifurcation curves T and the period-doubling bifurcation curves PD^1 [Fig. 8(e)]. Also, regions of complicated dynamics overlap less with the lockband. Although the detailed bifurcation structure near $G_1^{+(-)}$ is now different (Fig. 9), it includes TS points for example [Fig. 9(d)], the resulting effect of flipping bifurcations of periodic orbits emerging from $G_1^{+(-)}$ into the gap between the two lockbands is similar. In particular, the bifurcation diagrams in Figs. 9(a) and 7(a) for $\alpha = 0$, as well as these in Figs. 9(f) and 7(d) for $\alpha = 2$, are topologically equivalent.

The combined effect of α, Γ_E and Γ_N is clear from the rescaled Eqs. (10) and (11). There, the linewidth enhancement factor α appears in the product

$$\gamma\beta\alpha \times (\tilde{N} + 1) = \left(\frac{1}{2}\Gamma_E + \frac{c\Gamma\xi N_{\mathrm{ts}}}{n_{\mathrm{b}}}\right)\frac{\alpha}{\Gamma_N} \times \frac{N}{N_{\mathrm{thr}}}. \tag{14}$$

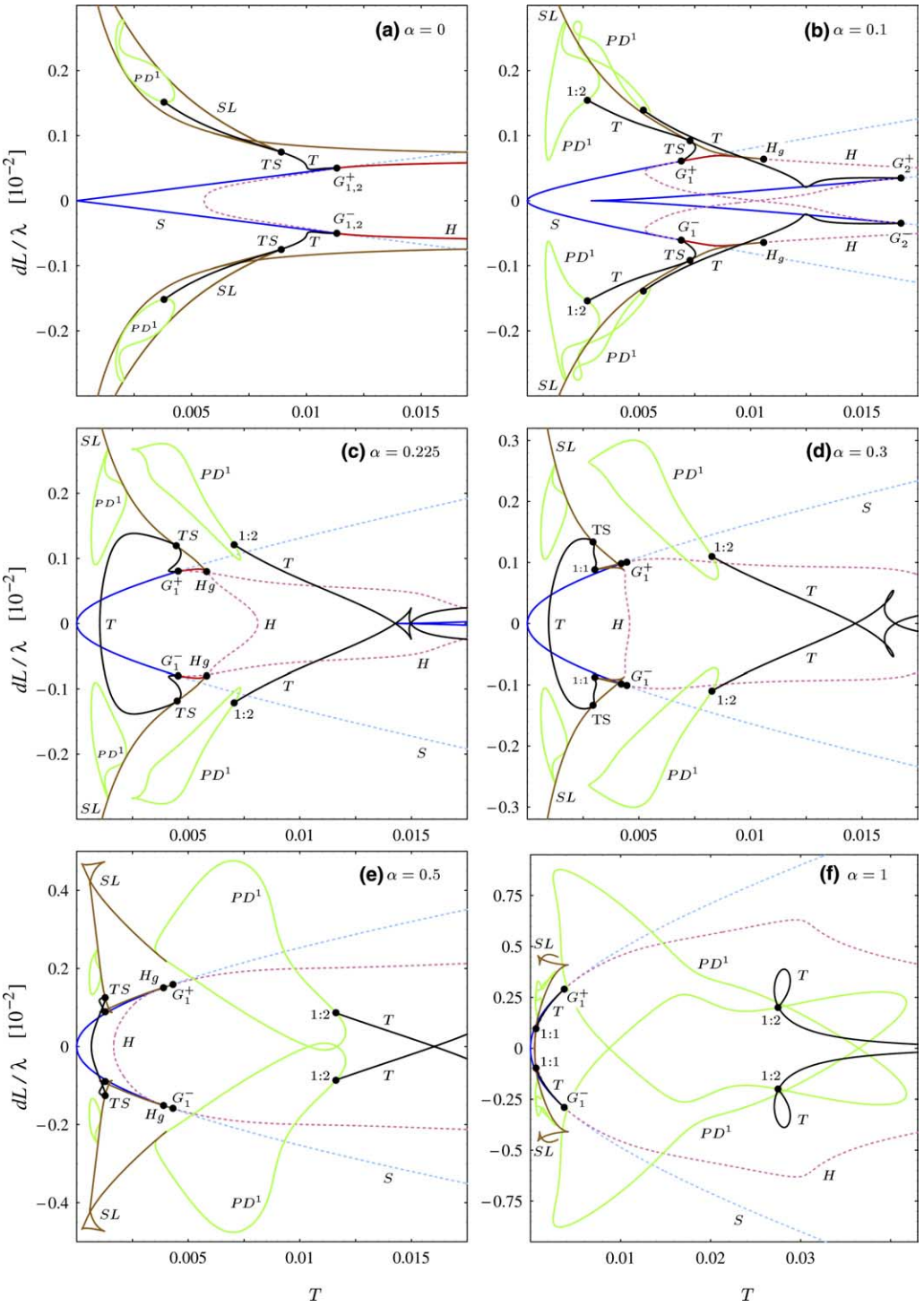

Fig. 8. Bifurcation diagram in the (T,dL/λ) plane for different values of the linewidth enhancement factor α. We use $L = 280$ μm, $\Gamma_E = 2 \times 10^{11}$ s^{-1}, $\Gamma_N = 10^9$ s^{-1}, and the color coding is as in Fig. 6.

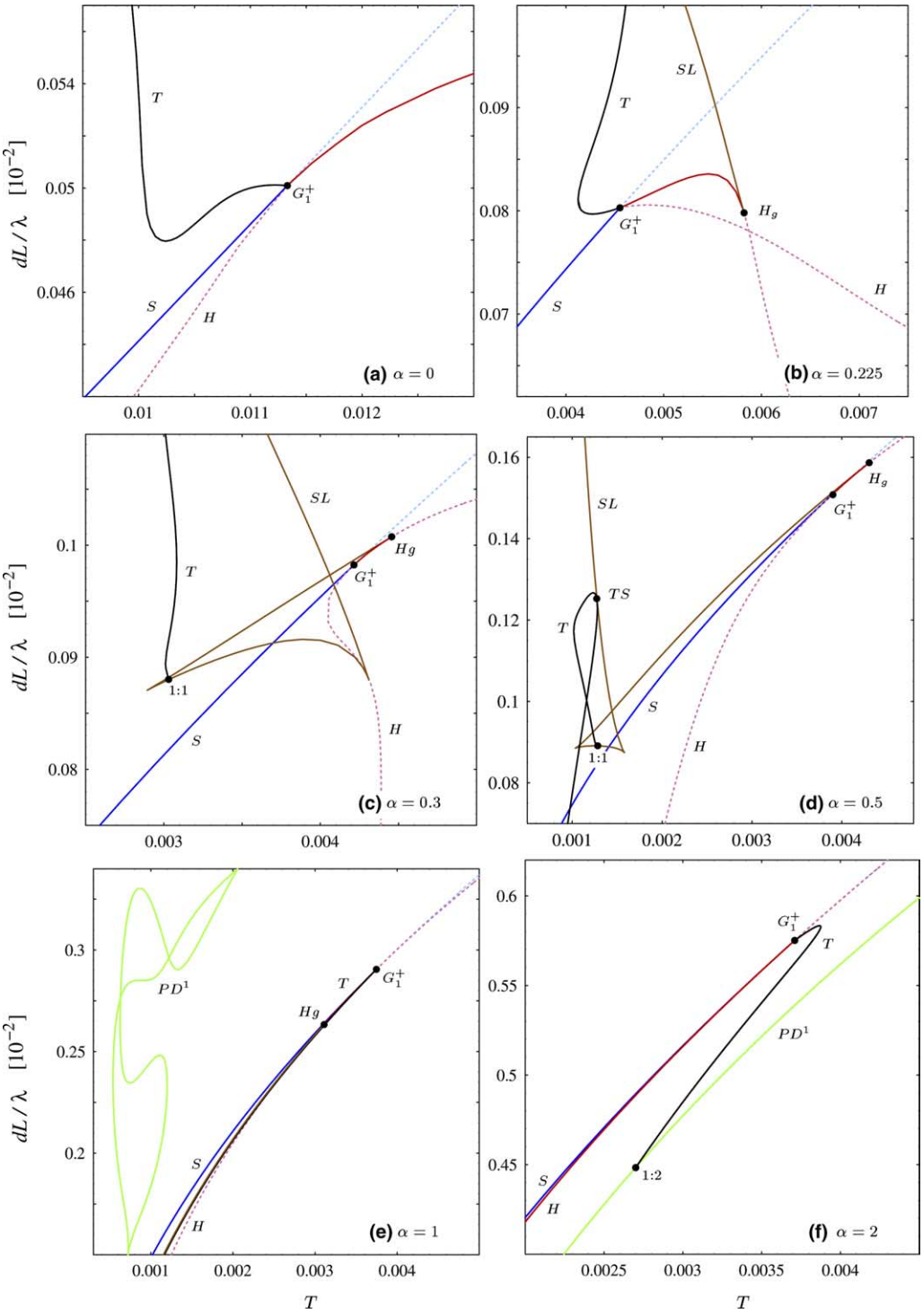

Fig. 9. Bifurcation diagram near saddle-node-Hopf point G_1^+ for different values of the linewidth enhancement factor α. We use $L = 280$ μm, $\Gamma_E = 2 \times 10^{11}$ s^{-1}, $\Gamma_N = 10^9$ s^{-1}, and the color coding is as in Fig. 6.

In coupled-cavity lasers, dynamical effects due to α may be amplified or inhibited depending on the decay rates Γ_E and Γ_N. It is interesting to note the difference between bidirectionally coupled lasers that are considered here and unidirectionally coupled (optically injected) lasers. In a rate equation model for an optically injected laser, the bifurcation diagram depends on Γ_E and Γ_N too. However, the very special situation where the Hopf curve has a cusp at the saddle-node-Hopf point G does not depend on Γ_E nor Γ_N. It always takes place for $\alpha = 1$ [51].

Throughout the paper, interesting phenomena appear for relatively low values of the optical coupling T (Figs. 6–9). A question may arise whether strong-coupling theory is really needed to understand coupled-laser behavior. For short-cavity lasers, several instabilities indeed appear at low T. However, some interesting changes take place at higher T and their analysis requires strong-coupling theory. For large α the instabilities associated with $G_2^{+(-)}$ migrate as far as $T \sim 0.5$ [Fig. 5(f)]. Furthermore, the lockband at high optical coupling still depends on α, Γ_E, and Γ_N. Fig. 4 shows changes to the lockband at high T with varying decay rates Γ_E and Γ_N. Most interestingly, even the low-T results found here cannot be reproduced with individual-cavity theory where the light of one laser is directly injected (with no changes to its phase) to the other laser. Finally, for longer-cavity lasers most of the interesting dynamics is expected at relatively high T [41].

5.2.3. Physical consequences of bifurcations

Bifurcation diagrams from Figs. 5–9 include information on regimes of stable and unstable coupled-laser operation for the entire range of optical-coupling strength, and different types of lasers. While it is practically impossible to make bifurcation diagram of a chaotic system, such as a composite-cavity laser, mathematically complete, the challenge is to find the key bifurcations that provide all the information interesting for a physicist. In order to extract these information, complicated looking bifurcation diagrams must be properly read.

Inside the lockband, that is marked by the left and right inclined patterns in Fig. 5, lasers are locked. Locked operation shows as a single-frequency peak in the spectra of both lasers. Outside the patterned region, lasers operate at two composite cavity modes and the output intensities oscillate. Away from green period-doubling curves and black torus bifurcation curves, the output intensity typically oscillates at a single frequency. This is represented by a periodic orbit of basic period. A laser spectrum in such region is discrete, it includes the main-frequency peak and side peaks detuned from the main-frequency by the frequency of this intensity oscillation. When lasers are operated in the region bounded by period-doubling curves or near torus bifurcation curves, the oscillation of the output intensity gets more complicated. Consequently, additional peaks appear in the laser spectra to the point where the spectrum becomes continuous – a hallmark of chaotic oscillation. Sometimes, T curves or PD curves overlap with the lockband, indicating bi- or multi-stability between locking and complicated dynamics. There, depending on the initial conditions, the laser settles to one of the two (or more) possible states. To illustrate intensity output at different regions of the bifurcation diagram, we plot attractors and the corresponding spectra of the intracavity electric fields for two different transitions across the bifurcation diagram. More examples of laser bifurcation transitions can be found in [52,53].

In Fig. 10, we fix $T = 0.05$, $\alpha = 0.5$, $\gamma = 10$, and sweep dL/λ across the torus bifurcation curve T and the lockband; compare with bifurcation diagrams in Figs. 5(c) and 6(c). For a large cavity-length mismatch, there is one periodic orbit [Fig. 10(a)]. As dL/λ is decreased, we cross the subcritical Hopf bifurcation and enter the lockband. A stable stationary point appears leading to bistability with the periodic orbit [Fig. 10(b)]. For these parameters, lasers can be either locked (point in the phase portrait and gray spectra) or unlocked (periodic orbit in the phase portrait and black spectra). The next bifurcation is the torus bifurcation T where the stable periodic orbit turns unstable and gives rise to torus [Fig. 10(c)]. Torus bifurcation introduces a new frequency in the intensity output. Spectra of quasiperiodic oscillation on a torus have contributions from the two frequencies involved, and from their linear super-

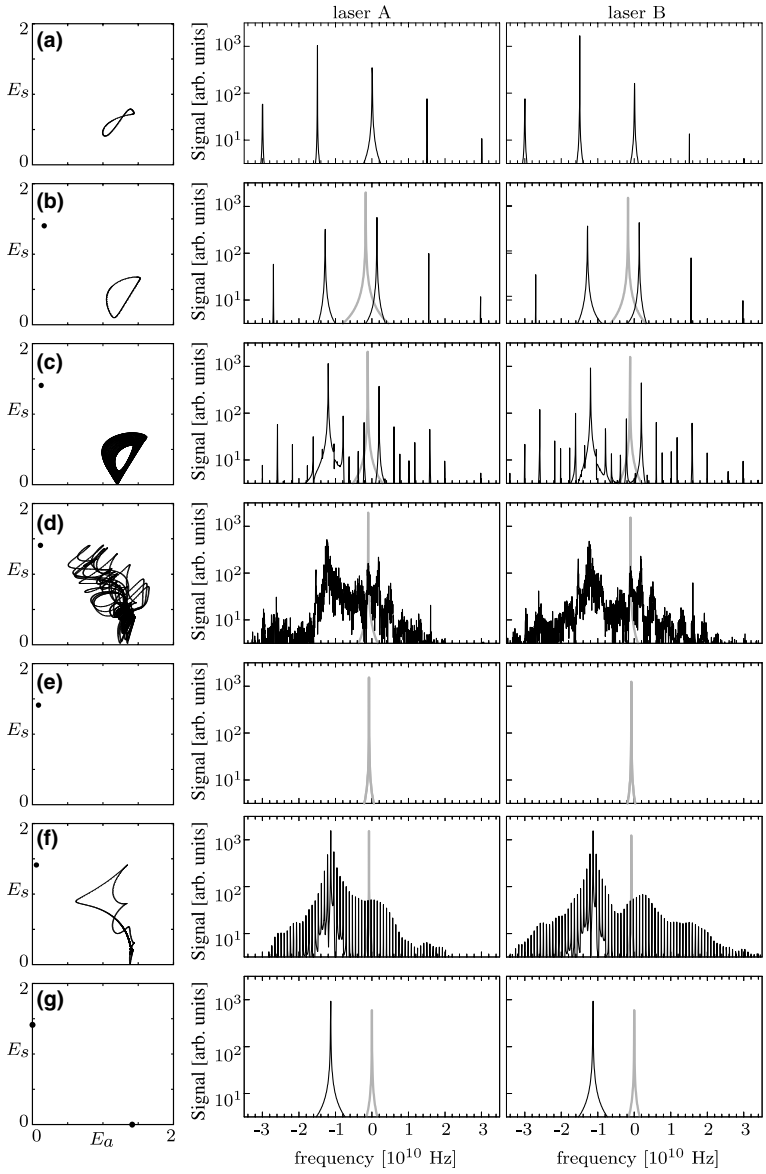

Fig. 10. (first column) Phase portraits and spectra of the intracavity electric field in lasers (second column) A and (third column) B for a bifurcation transition at fixed $T = 0.05$, $\alpha = 0.5$, $\gamma = 10$, and varying cavity-length mismatch dL/λ. From (a) to (g) dL/λ [10^{-2}] = 0.5, 0.3, 0.22, 0.2, 0.15, 0.1, and 0.0. In case of bistability, laser spectra associated with two different attractors are overlaid. The spectra corresponding to the stationary point with large E_S component is plotted in gray. Compare with the bifurcation diagrams in Figs. 5(c) and 6(c).

positions. Below T, the torus breaks-up into chaotic attractor [Fig. 10(d)]. There, lasers exhibit bistability between locking and chaos. The chaotic attractor is subsequently destroyed in a homoclinic tangency [not shown in Fig. 6(c)] that originates from the nearby 1:2 resonance point. Then, the stationary point is the only stable solution [Fig. 10(e)]. Note that the birth of torus, the break-up into chaotic attractor, and disappearance of the chaotic attractor, all take place inside the

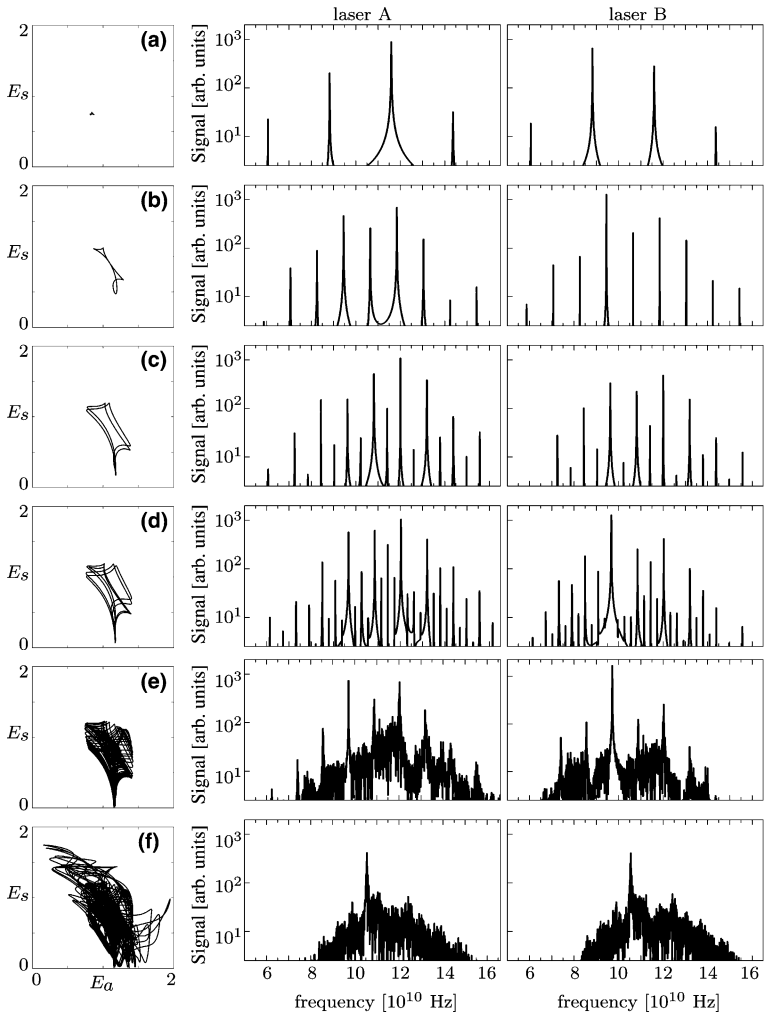

Fig. 11. (first column) Phase portraits and spectra of the intracavity electric field in lasers (second column) A and (third column) B for a bifurcation transition at fixed $T = 0.07$, $\alpha = 2$, $\gamma = 10$, and varying cavity-length mismatch dL/λ. From (a) to (f) dL/λ [10^{-2}] = 1.5, 1.3, 1.1, 1.05, 1.0, and 0.0. The reference frequency is the same as in Fig. 10. Compare with the bifurcation diagrams in Figs. 5(e) and 6(e). Note the absence of locking.

lockband. When dL/λ is further decreased, a new periodic orbit appears [Fig. 10(f)] via saddle-node-of-periodic-orbit bifurcation [not shown in Fig. 6(c)]. This orbit is also involved in the global saddle-node bifurcation (taking place at the solid blue part of S). The corresponding spectra have a large peak where locking will subsequently occur, and shoulders of lower peaks, which is characteristic near phase locking. At S, two stationary points, one of which is stable, are born on this periodic orbit and we enter bistable lockband with two stable stationary points. Each of the two pints corresponds to a single frequency operation [Fig. 10(g)].

In Fig. 11, we fix $T = 0.07$, $\alpha = 2$, $\gamma = 10$, and sweep dL/λ across the period-doubling cascade; compare with the bifurcation diagrams in Figs. 5(e) and 6(e). A tiny periodic orbit at large dL/λ indicates that lasers operate close to being independent of each other [Fig. 11(a)]. Upon decreasing the cavity-length mismatch, period-doubling bifurcation is encountered and the orbit of basic

period gives rise to an orbit of twice the basic period [Fig. 11(b)]. As a consequence, additional peaks appear in the spectra at half the beatnote. This is the first step in an infinite period-doubling cascade [Fig. 11(c) and (d)] that leads to a 'small' chaotic attractor with strong periodic components [Fig. 11(e)]. As dL/λ is further decreased, the 'small' chaotic attractor hits a saddle orbit within its basin of attraction and expands significantly [Fig. 11(f)]. This bifurcation transition shows the appearance of complicated laser dynamics for the coupling strength at which no locking is possible.

5.3. Organizing centers

The bifurcation diagram of a coupled-cavity laser includes an enormous amount of bifurcations. Since not all of them are equally important, we extracted the key bifurcation curves that form the backbone of the coupled-cavity laser dynamics. A number of organizing centers were found but a detailed study of them is beyond the scope of this work. Let us list these points and briefly discuss the other interesting bifurcations to be expected in their vicinity. The 1:1 and 1:2 resonances are well understood [45]. The 1:1 resonance point gives rise to a homoclinic tangency bifurcation curve along which a chaotic attractor, due to the break-up of a 2-torus, is destroyed. The simpler of the two types of the 1:2 resonance involves a heteroclinic tangency bifurcation curve where a chaotic attractor, due to the break-up of a 2-torus, is destroyed. Organizing centers associated with period-doubling curves often come in cascades like PD^n curves. The other type of 1:2 resonance may be associated with a 1:2 resonance cascade. Complete unfolding for cascades of 1:2 resonances is the topic of ongoing investigation. A partial numerical unfolding was presented for an example of an optically injected laser [49]. These numerical studies revealed the existence of a homoclinic tangency curve along which the chaotic attractor, due to the period-doubling cascade, is destroyed. Cascades of B_n points have been recently studied in detail (see [50] and references therein) to find their scaling constants that are different from the well-known Feigenbaum constant for the period-doubling cascade itself. In particular, the saddle-node-of-periodic-orbit curve is expected in the vicinity of B_n cascade. Another organizing center associated with period-doubling bifurcation, so called fold-flip bifurcation point, appears when a PD curve becomes tangent to an SL curve [54]. A number of fold-flip points were found here. They can be clearly seen in Fig. 8 but we did not mark them for clarity reasons. The most complicated dynamics are to be found near saddle-node-of-periodic-orbit-torus points TS. Such points have been studied only recently in an abstract discrete map [55]. A resonance tongue structure associated with 2-torus born along T, and chaotic dynamics due to the break-up of this 2-torus are expected. Another torus bifurcation curve is expected where the 2-torus bifurcates into a 3-torus. Also, there must be a resonance tongue structure associated with the dynamics on this 3-torus, as well as chaotic dynamics due to the break-up of the 3-torus. TS points should also be found in the model of an optically injected laser with modulated current.

5.4. Varying cavity-length

Dynamics of coupled-cavity lasers, in particular the positions of organizing centers $G_{1,2}^{+,-}$ and

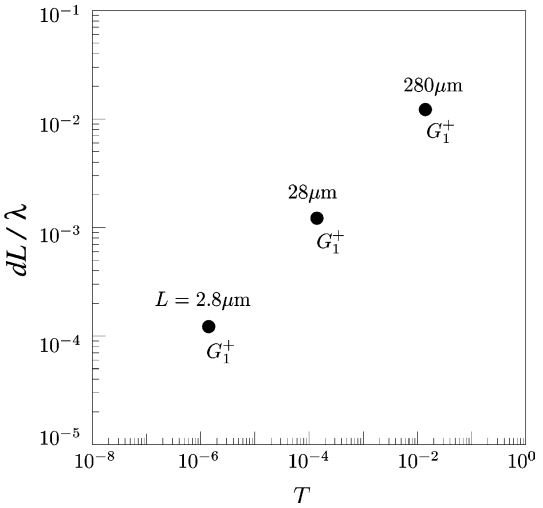

Fig. 12. With decreasing cavity-length L, codimension-two saddle-node-Hopf points G_1 shift towards the origin of the $(T,dL/\lambda)$ plane. So do the associated instabilities. For this figure $\alpha = 2$, $\Gamma_E = 10^{11}$ s^{-1}, and $\Gamma_N = 5 \times 10^9$ s^{-1}.

associated instabilities, strongly depend on the cavity length L. In the (T,dL/λ) plane, instabilities and chaos appear where there is strong composite-mode coupling and the composite-mode beat note approaches the relaxation oscillation frequency. Starting at longer cavity length, two important changes take place as L is decreased. First, the composite-mode beat note can coincide with the relaxation oscillation frequency at smaller T values for given dL/λ. Second, at these small T values, strong composite-mode coupling occurs over a significantly narrower range of dL/λ (Fig. 2). These changes lead to $G_1^{+(-)}$ and associated instabilities shift with decreasing L towards the origin of the (T,dL/λ) plane (Fig. 12). Consequently, for microcavities ($L = 2.8$ μm) chaos may appear at ultrasmall values of $T \sim 10^{-6}$ [24], where nonlinearities associated with the resonator coupling are appreciable (Fig. 2). This indicates a difference in the signatures of dynamical behavior of long and short coupled-cavity lasers.

The result is obtained by modeling the coupling between lasers as a dielectric 'bump'. It would be interesting to see how the interplay between the modal and gain nonlinearities, leading to chaotic dynamics, manifests for a different coupling model. One example would be to use a refractive index function that takes different values in different sections of a composite-laser system, and has finite discontinuities at the interfaces between different sections.

6. Conclusions

The paper provides a global view of the dynamics of coupled-cavity class-B lasers within the framework of composite-cavity mode theory. We explained, for different ratios between the photon and population decay rates, how the overall dynamical picture transforms with increasing linewidth enhancement factor α. In particular, an uninterrupted and degenerate (bistable) lockband at $\alpha = 0$ unfolds and develops a gap which is gradually occupied with instabilities and chaos for $\alpha \neq 0$. The underlying mechanism is a change in the competition between composite-cavity modes causing a change in the type of codimension-two saddle-node-Hopf points. Furthermore, several other codimension-two bifurcations, including strong resonances and saddle-node-of-periodic-orbit-torus bifurcation, are identified to be sources of instabilities and chaos in coupled-cavity lasers. We found that the complexity of the bifurcation diagram due to the linewidth enhancement factor α can be either enhanced or inhibited depending on the ratio between the photon and population decay rates. The dependence of the dynamics on the cavity-length reveals effects due to nonlinear optical coupling. With decreasing cavity-length the conditions necessary for the complicated dynamics to occur shift towards the origin of the (T,dL/λ) parameter space. Consequently, in microcavity lasers chaotic oscillations appear for vanishing optical coupling [24], where lasers are generally expected to act independently. In this way our work provides new insight into an overall understanding of coupled-laser behavior.

This work is partially funded by the United States Department of Energy under contract DE-AC04-94AL8500. WC acknowledges support from the Research Award of the Alexander von Humboldt Foundation.

References

[1] N.G. Basov, E.M. Belenov, V.D. Letokhov, Sov. Phys. Tech. Phys. 10 (1965) 845.
[2] M.B. Spencer, W.E. Lamb Jr., Phys. Rev. A 5 (1972) 884.
[3] M.B. Spencer, W.E. Lamb Jr., Phys. Rev. A 5 (1972) 893.
[4] W.W. Chow, Opt. Lett. 10 (1985) 442.
[5] W.W. Chow, JOSA B 3 (1986) 833.
[6] W.W. Chow, IEEE J. Quant. Electron. QE-22 (1986) 1174.
[7] W.J. Fader, IEEE J. Quant. Electron. 21 (1985) 1838.
[8] A.P. Napartovich, Proc. SPIE 2109 (1993) 341.
[9] W.T. Tsang, N.A. Olsson, R.A. Logan, Electron. Lett. 19 (1983) 488.
[10] R.A. Elliott, R.K. DeFreez, T.L. Paoli, R.D. Burnham, W. Streifer, IEEE J. Quant. Electron. 21 (1985) 598.
[11] H.G. Winful, S.S. Wang, Appl. Phys. Lett. 52 (1988) 1774.
[12] K.S. Thornburg Jr., M. Moller, R. Roy, T.W. Carr, R.D. Li, T. Erneux, Phys. Rev. E 55 (1997) 3865.
[13] A.I. Khibnik, Y. Braiman, T.A.B. Kennedy, K. Wiesenfeld, Physica D 111 (1998) 295.
[14] G.C. Dente, C.E. Moeller, P.S. Durkin, IEEE J. Quant. Electron. 26 (1990) 1014.
[15] R. Li, T. Erneux, Opt. Commun. 99 (1993) 196.
[16] A. Hohl, A. Gavrielides, T. Erneux, V. Kovanis, Phys. Rev. Lett. 78 (1997) 4745.

[17] T. Heil, I. Fischer, W. Elsäßer, Phys. Rev. Lett. 86 (2001) 795.
[18] J. Mulet, C. Masoller, C.R. Mirasso, Phys. Rev. A 65 (2002) 063815.
[19] J. Javaloyes, P. Mandel, D. Pieroux, Phys. Rev. E 67 (2003) 036201.
[20] H. Erzgräber, D. Lenstra, B. Krauskopf, I. Fischer, Proc. SPIE 5452 (2004) 352.
[21] H. Erzgräber, D. Lenstra, B. Krauskopf, E. Wille, M. Peil, I. Fischer, W. Elsäßer, Applied Nonlinear Mathematics Research Report 2004, University of Bristol. Available from: <http://www.enm.bris.ac.uk/anm/preprints/2004r20.html>.
[22] E. Wille, M. Peil, I. Fischer, W. Elsäßer, Proc. SPIE 5452 (2004) 41.
[23] S. Yanchuk, K. Schneider, L. Recke, Phys. Rev. E 69 (2004) 056221.
[24] S. Wieczorek, W.W. Chow, Phys. Rev. Lett. 92 (2004) 213901.
[25] A.J. Fischer, K.D. Choquette, W.W. Chow, A.A. Allerman, D.K. Serkland, K.M. Geib, Appl. Phys. Lett. 79 (2001) 4079.
[26] Y. Liu, H.K. Liu, Y. Braiman, Appl. Opt. 41 (2002) 5036.
[27] A.A. Tager, IEEE Photon. Technol. Lett. 6 (1994) 164.
[28] H. Wenzel, U. Bandelow, H.J. Wunnsche, J. Rehberg, IEEE J. Quant. Electron. 32 (1996) 69.
[29] G.D. VanWiggeren, R. Roy, Science 279 (1997) 1198.
[30] F.Y. Lin, J.M. Liu, IEEE J. Quant. Electron. 40 (2004) 682.
[31] S.A. Shakir, W.W. Chow, Opt. Lett. 9 (1984) 202.
[32] E. Kapon, J. Katz, A. Yariv, Opt. Lett. 10 (1984) 125.
[33] P. Mandel, L. Ruo-ding, T. Erneux, Phys. Rev. A 39 (1989) 2502.
[34] V. Zehnle, Phys. Rev. A 62 (1997) 033814.
[35] U. Bandelow, M. Wolfrum, J. Sieber, M. Radziunas, IEEE J. Quant. Electron. QE-37 (2001) 183.
[36] C.R. Mirasso, M. Kolesik, M. Matus, J.K. White, J.V. Moloney, Phys. Rev. A 65 (2001) 013805.
[37] M. Sargent III, M.O. Scully, W.E. Lamb Jr., Laser Physics, Addison-Wesley, New York, 1974.
[38] R. Roy, K.S. Thornburg Jr., Phys. Rev. Lett. 72 (1994) 2009.
[39] K. Otsuka, R. Kawai, S.-L. Hwong, J.-Y. Ko, J.-L. Chern, Phys. Rev. Lett. 84 (2000) 3049.
[40] O. Ushakov, S. Bauer, O. Brox, H.J. Wünsche, F. Henneberger, Phys. Rev. Lett. 92 (2004) 043902.
[41] S. Wieczorek, W.W. Chow, Phys. Rev. A 69 (2004) 033811.
[42] C.L. Tang, H. Statz, G. DeMars, J. Appl. Phys. 34 (1963) 2289.
[43] E. Doedel, T. Fairgrieve, B. Sandstede, A. Champneys, Yu. Kuznetsov, X. Wang, AUTO 2000: Continuation and bifurcation software for ordinary differential equations. Available from: <http://sourceforge.net/projects/auto2000/>.
[44] W.W. Chow, S.W. Koch, Semiconductor-Laser Fundamentals: Physics of the Gain Materials, Springer-Verlag, Berlin Heidelberg, 1999.
[45] Yu.A. Kuznetsov, Elements of Applied Bifurcation Theory, Springer, New York, 1995.
[46] S. Wieczorek, W.W. Chow, Bistable analytic-phase synchronization in strongly competing chaotic lasing models, submitted.
[47] E. Ott, Chaos in Dynamical Systems, Cambridge University Press, Cambridge, 1993.
[48] M. Feigenbaum, J. Stat. Phys. 19 (1978) 25.
[49] S. Wieczorek, B. Krauskopf, D. Lenstra, Phys. Rev. E 64 (2001) 056204.
[50] B. Oldeman, B. Krauskopf, A.R. Champneys, Physica D 146 (2000) 100.
[51] S. Wieczorek, B. Krauskopf, D. Lenstra, Opt. Commun. 172 (1–6) (1999) 279.
[52] B. Krauskopf, S. Wieczorek, D. Lenstra, Appl. Phys. Lett. 77 (11) (2000) 1611.
[53] S. Wieczorek, T.B. Simpson, B. Krauskopf, D. Lenstra, Opt. Commun. 215 (2003) 125.
[54] Yu.A. Kuznetsov, H.G.E. Meijer, L. van Veen, The fold-flip bifurcation, Preprint nr. 1270, Department of Mathematics, Universiteit Utrecht, The Netherlands, 2003.
[55] R. Vitolo, Bifurcations of attractors in 3D diffeomorphisms, Ph.D. thesis, Rijksuniversiteit Groningen, The Netherlands.